Evaluation of 6-D Reaction Integrals via Double Application of the Divergence Theorem

Evaluation of 6-D Reaction Integrals via Double Application of the Divergence Theorem

J. Rivero, F. Vipiana, *Senior Member, IEEE*, D. R. Wilton, *Life Fellow, IEEE*, W. A. Johnson, *Senior Member, IEEE*

***Abstract*—This paper addresses the problem of efficiently and accurately evaluating the singular or near-singular double volume (6-D) reaction integrals fundamental to the solution of volume integral equations (VIEs) using the method of moments (MoM). VIE techniques based on the MoM are used to obtain accurate solutions for electromagnetic (EM) problems of all types, and the accurate computation of the singular and near-singular reaction integrals that occur in the resulting system matrices is crucial for accurate EM modeling. Here we propose a scheme to treat, as a whole, the 6-D reaction integrals appearing in the MoM. The divergence theorem is directly applied twice in the physical space domain, not a transformed domain, thus eliminating restrictions to well-shaped elements. With appropriate integration reordering, the 6-D volume integrals are expressed as two radial integrals followed by two surface integrals over source and observation domain boundaries. We further smooth the integral by removing the static form of the kernel and evaluating it separately using a semi-analytical approach. The method is numerically validated for static and dynamic kernels arising in the electric field volume integral equations (i.e., for kernels having $1/R$ singularities) and for linear basis functions.**

***Index Terms*—integral equations, moment methods, numerical analysis, divergence theorem, singular integrals.**

I. Introduction

One of the most widespread formulations for modeling 3-D electromagnetic problems involving inhomogeneous materials is the volume integral equation (VIE), solved either via the method of moments (MoM) [1], Nyström's method [2], or point-matching schemes [3]. VIE has been used in a number of direct and inverse scattering applications, ranging from the study of propagation in rain [4] to geological prospecting [5], and from integrated circuit analysis [6] to medical applications [7]–[9]. The VIE, unlike the finite element method (FEM), automatically accounts for radiation conditions at infinity, and is not limited to isotropic and piecewise homogeneous materials, unlike most surface integral equation (SIE) formulations [10], [11]. However, the rigorous solution of radiation and scattering problems using VIEs requires the accurate and efficient numerical evaluation of double volume (6-D) reaction integrals. The usual strategies for handling the singular or near-singular volumetric integrals arising in VIE-MoM extend the well-known techniques for surface integrals, i.e., singularity subtraction [12] and singularity cancellation [13]. Recently, some techniques to reduce the inner volumetric integral to lineal integrals has been published [14]. However, these methods focus on carefully treating the inner source integral, then numerically evaluating the outer test integral; however, the outer test integral can still present a (low-order) singular behavior.

Knockaert first suggested using appropriate integral theorems to handle both source and test integrals [15], but simply outlined the approach as applied to 4-D problems with scalar static and free-space kernels, and without specifically addressing the full 6-D integration problem for both vector and scalar potentials. More recently, Bleszynski et al. presented a method allowing the analytical conversion of matrix element expressions for volumetric integral equation formulations with tensor and vector homogeneous media Green's functions from 6-D volumetric to 4-D surface integrals with non-singular integrands [16]. Their approach, implemented specifically for SWG basis functions [17], was expressed in terms of surface integrals over the various face-pair combinations associated with a source and test tetrahedral element pair. The surface integrals were evaluated numerically, but their convergence properties were not investigated. Polimeridis et al. have also presented a method based on interchanging integration order to first perform radial integrals for the source and observation point integrals followed by integration around element boundaries [18]. Their treatment was limited to self-interacting, edge-adjacent, or vertex-adjacent elements, and to well-shaped element pairs. More recently, Reid extended the generalized Taylor–Duffy strategy to handle the singular volumetric integral pair arising in VIE-MoM [19].

The work here extends the authors' approach of [20], [21] in which the divergence theorem was applied twice to evaluate the double surface (4-D) integrals arising in the MoM solution of surface integral equations (SIEs). The result was a pair of inner radial integrals that could be evaluated either numerically or in closed form, plus a pair of contour integrals around the boundaries of a source and test triangular element pair. Here, however, the divergence theorem is applied to the double volume (6-D) reaction integrals that appear in the MoM solution of VIEs. In contrast to [20], here there

Manuscript received xxxxxxx, 2020; revised xxxxxxx; accepted xxxxxxx. Date of publication xxxxxxx; date of current version xxxxxxx. This work was supported by the Italian Ministry of University and Research under the PRIN project "BEST-Food, Broadband Electromagnetic Sensing Technologies for Food quality and security assessment". *(Corresponding author: Francesca Vipiana.)*

J. Rivero and F. Vipiana are with the Department of Electronics and Telecommunications, Politecnico di Torino, 10129 Torino, Italy (email: javier.rivero@polito.it; francesca.vipiana@polito.it).

D. R. Wilton is with the Department of Electrical and Computer Engineering, University of Houston, Houston, TX 77204-4005 USA (email: wilton@uh.edu).

W. A. Johnson is an electromagnetics consultant in Jemez Springs, NM 87025, USA (e-mail: w.johnson24@comcast.net).

Color versions of one or more of the figures in this communication are available online at http://ieeexplore.ieee.org.

Digital Object Identifier xxxxxxxxxxxxxxxxxxxx

is no need to project source domains onto test domains or vice versa, simplifying application of the divergence theorem. The resulting integrals consist of two radial integrals and two surface (4-D) integrals for arbitrarily located (source and test) volumetric element pairs. For polynomial bases and homogeneous media Green's functions, the radial integrals can be evaluated in closed form; for more complex bases or kernels (e.g., for layered or periodic media), they can also be performed numerically. Since elements are not pre-mapped to standardized shapes, the scheme is also quite general, i.e., not limited to well-shaped elements nor to ad-hoc treatments for self-, edge-, or vertex-adjacent geometries. Here we illustrate the approach using homogeneous media Green's functions and SWG bases defined on tetrahedral elements, and we evaluate the radial integrals analytically. Finally, for the static kernel case and SWG bases, the initial 6-D integral is further reduced by two dimensions by exact integration in 2-D, leaving only a 2-D integral to be performed numerically; this result is also used to accelerate the convergence of the proposed scheme for dynamic kernels and SWG bases.

The paper is structured as follows. In Sect. II, the general expression for the double application of the volume divergence theorem is derived. Section III is devoted to the evaluation of the radial integrals, while Sect. IV deals with the semi-analytical evaluation of the static kernel with SWG bases, used then in Sect. V to accelerate the convergence of the integration for the dynamic kernel case. In Sect. VI several numerical results are presented, and finally, Sect. VII discusses conclusions and possible extensions of the approach. Preliminary numerical results were recently presented in [22]–[24].

II. Double Application of the Volume Divergence Theorem

Let us consider the 6-D integral

$$I_{V,V'} = \int_V \int_{V'} F(\mathbf{r},\mathbf{r}')\, dV' dV, \tag{1}$$

where $F(\mathbf{r},\mathbf{r}')$ typically takes the form

$$F(\mathbf{r},\mathbf{r}') = t(\mathbf{r}) G(\mathbf{r},\mathbf{r}') b(\mathbf{r}'), \tag{2}$$

with $t(\mathbf{r})$ either a scalar or a vector component of a test basis function, and $b(\mathbf{r}')$ a similarly defined (source) basis function. $G(\mathbf{r},\mathbf{r}')$ is either a scalar or a component of a dyadic Green's function, and V and V' are the volumetric domains of tetrahedral test and source basis functions, respectively.

Applying the divergence theorem to both the source and test integrations, as in [25], the integral (1) can be written as

$$I_{V,V'} = \oint_S \oint_{S'} \left[\frac{(\hat{\mathbf{n}}\cdot\hat{\mathbf{R}})(\hat{\mathbf{n}}'\cdot\hat{\mathbf{R}}')}{R^2} \times \int_0^R \int_0^{R_{S'}} F(\mathbf{r},\mathbf{r}') R'^2 dR'\, dR_{S'} \right] dS' dS. \tag{3}$$

Since $\mathbf{r}$ and $\mathbf{r}'$ in (3) vary radially along lines between point pairs defined on the boundaries of the source and test tetrahedra of the outer integrals in (3), it is convenient to first define point pairs $\mathbf{r}'_{S'}$ and $\mathbf{r}_S$ on the source and test boundaries, resp., then parameterize the positions of $\mathbf{r}$ and $\mathbf{r}'$ along the line connecting them. Note that the *extended* line between points $\mathbf{r}'_{S'}$ and $\mathbf{r}_S$ on the tetrahedral boundaries generally intersects each source and test surface twice, defining up to four radial integration paths, each distinguished by a different endpoint pair, but with overlapping domains. The signs of $\hat{\mathbf{n}}'\cdot\hat{\mathbf{R}}'$ and $\hat{\mathbf{n}}\cdot\hat{\mathbf{R}}$ in (3) determine the sign of each endpoint pair's radial path integral contribution, and contributions from overlapping portions of domains *outside* the original tetrahedrons must necessarily cancel. For very well-separated elements, this implies that severe cancellation errors arising from the computation of small differences of large numbers can result, limiting the approach's usefulness to self- and nearby-element interactions. We assume a unit normal $\hat{\mathbf{n}}'$ is associated with the point $\mathbf{r}'_{S'}$ on the boundary S' of the tetrahedral (source) volume V', as shown in Fig. 1; similar definitions apply to the unprimed (test) quantities. We also define the quantities $\hat{\mathbf{R}} = -\hat{\mathbf{R}}' = (\mathbf{r}_S - \mathbf{r}'_{S'})/R$, $R = |\mathbf{r}_S - \mathbf{r}'_{S'}|$, and $\mathbf{r}' = \mathbf{r} + R'\hat{\mathbf{R}}'$, $R' = |\mathbf{r}' - \mathbf{r}|$, $0 \le R' \le R_{S'} = |\mathbf{r} - \mathbf{r}'_{S'}|$, and $\mathbf{r} = \mathbf{r}'_{S'} + R_{S'}\hat{\mathbf{R}}$, $0 \le R_{S'} \le R$. The interchange of integration order in (3) is permitted by the independence of the observation and source coordinate variables and their associated domains. The resulting representation has features in common with those of [26], with two inner radial integrals and two outer integrals over source and test element surfaces. For tetrahedral source and test domains, the outer surface

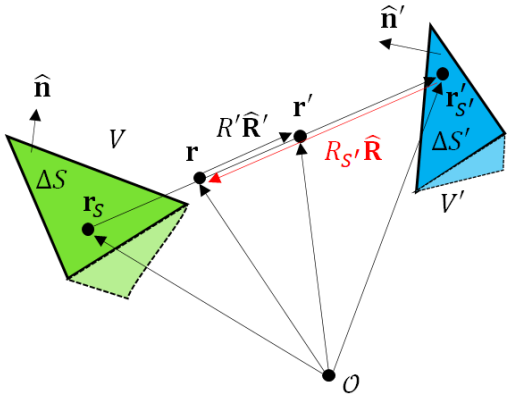

Fig. 1. The orientation of a pair of tetrahedral elements in space and the definition of quantities for the computation of radial integrals associated with a pair of interacting surface $\Delta S'$ and ΔS for source V' and test V tetrahedral, respectively.

integrals in (3) can be evaluated by considering contributions from all the pairs of interacting source and test faces of the tetrahedrons; hence, (3) can be evaluated as a sum of face-pair contributions of the form

$$I_{\Delta S_i,\Delta S'_j} = \int_{\Delta S_i} \int_{\Delta S'_j} \left[\frac{(\hat{\mathbf{n}}\cdot\hat{\mathbf{R}})(\hat{\mathbf{n}}'\cdot\hat{\mathbf{R}}')}{R^2} \times \int_0^R \int_0^{R_{S'}} F(\mathbf{r},\mathbf{r}')\, R'^2 dR'\, dR_{S'} \right] dS'_j\, dS_i, \tag{4}$$

where ΔS_i and $\Delta S'_j$ are a pair of test and source faces, respectively. Note that interactions between *coplanar* face pairs vanish since both dot products in (4), $\hat{\mathbf{n}} \cdot \hat{\mathbf{R}}$ and $\hat{\mathbf{n}}' \cdot \hat{\mathbf{R}}'$, vanish. The inner, radial integrals in (4),

$$I_R = \int_0^R \int_0^{R_{S'}} F(\mathbf{r}, \mathbf{r}')\, R'^2 dR'\, dR_{S'}, \tag{5}$$

may be evaluated in closed form for dynamic and static cases, as well as for free space Green's functions G and ∇G, with or without the presence of polynomial vector bases, as detailed in Sect. III.

To analyze the two outer surface integrals, we apply variable transformations for both surfaces. Defining

$$\mathcal{F}(\mathbf{r}, \mathbf{r}') = \frac{(\hat{\mathbf{n}} \cdot \hat{\mathbf{R}})(\hat{\mathbf{n}}' \cdot \hat{\mathbf{R}}')}{R^2} I_R, \tag{6}$$

the contribution to the boundary integral (3) of a single face pair, ΔS and $\Delta S'$, can be written as

$$\begin{aligned} I_{\Delta S, \Delta S'} &= \int_{\Delta S} \int_{\Delta S'} \mathcal{F}(\mathbf{r}, \mathbf{r}')\, dS'\, dS \\ &= \int_z \int_\rho \int_{z'} \int_{\rho'} \mathcal{F}(z, \rho, z', \rho') d\rho' dz' d\rho\, dz, \end{aligned} \tag{7}$$

where the surfaces ΔS and $\Delta S'$ are parameterized with respect to a local cylindrical z-axis defined along the intersection of the planes containing ΔS and $\Delta S'$. The cylinder axis $\hat{\mathbf{z}}$ is defined as $\hat{\mathbf{z}} = (\hat{\mathbf{n}} \times \hat{\mathbf{n}}')/|\hat{\mathbf{n}} \times \hat{\mathbf{n}}'|$ and the vectors $\hat{\boldsymbol{\rho}}$ and $\hat{\boldsymbol{\rho}}'$ are orthogonal to the intersection line and the normals to the planes containing the surfaces ΔS and $\Delta S'$, respectively, as shown in Fig. 2. The vectors $\hat{\boldsymbol{\rho}}$ and $\hat{\boldsymbol{\rho}}'$ are defined as $\hat{\boldsymbol{\rho}} = (\hat{\mathbf{n}} \times \hat{\mathbf{z}})/|\hat{\mathbf{n}} \times \hat{\mathbf{z}}|$ and $\hat{\boldsymbol{\rho}}' = (\hat{\mathbf{n}}' \times \hat{\mathbf{z}})/|\hat{\mathbf{n}}' \times \hat{\mathbf{z}}|$. Due to the independence of the observation and source coordinate variables and their associated domains, we can reorder the integral (7) as

$$I_{\Delta S, \Delta S'} = \int_{z_L}^{z_U} \int_{z'_L}^{z'_U} \int_{\rho_L(z)}^{\rho_U(z)} \int_{\rho'_L(z')}^{\rho'_U(z')} \mathcal{F}(z, \rho, z', \rho') d\rho' d\rho\, dz' dz. \tag{8}$$

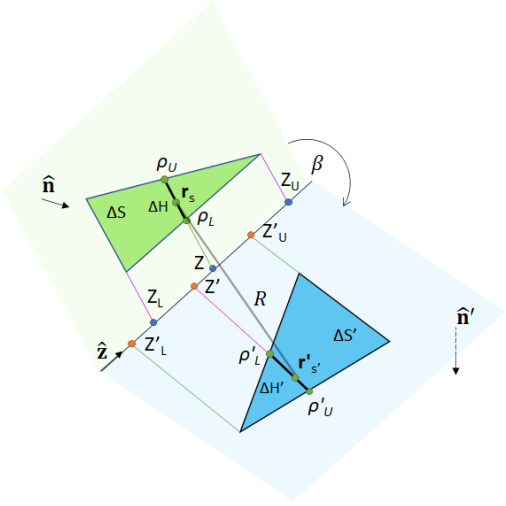

Fig. 2. Geometrical definition of the limits in (7) and the dependence of the ρ and ρ' limits on z and z'.

In this local cylindrical coordinate system, R and the dot product terms in (6) can be written as

$$\begin{aligned} R &= \sqrt{\rho^2 + \rho'^2 - 2\rho\rho' \cos\beta + \Delta z^2}, \\ \hat{\mathbf{n}} \cdot \hat{\mathbf{R}} &= -\frac{\rho' \sin(\beta)}{R}, \\ \hat{\mathbf{n}}' \cdot \hat{\mathbf{R}}' &= \frac{\rho \sin(\beta)}{R}, \end{aligned} \tag{9}$$

where $\Delta z = z - z'$, and β is the angle between the two planes containing the observation and source surface integration domains, computed as $\beta = \mathrm{atan2}[\hat{\mathbf{z}} \cdot (\hat{\mathbf{n}} \times \hat{\mathbf{n}}'), (\hat{\mathbf{n}} \cdot \hat{\mathbf{n}}')]$.

Though a given tetrahedral face-pair configuration may appear quite different than in Fig. 2, the equations defining axes, normals, etc. are general, and the relative positions and orientations of the parent tetrahedral pairs are arbitrary. If two vertices of a triangle project onto the same point along the line of intersection of the source and test triangle planes, as shown for the triangle at left in Fig. 3, then both the integrand and the limits vary smoothly with z; hence the triangle may be integrated using a single dyadic product of independent z and ρ Gauss-Legendre (GL) rules. But the limits do not vary smoothly for the more general case, shown at right in the figure; there the projection lines subdivide the triangle into two subtriangles, for each of which the integral must be independently evaluated and the integrals summed to make effective use of GL rule properties.

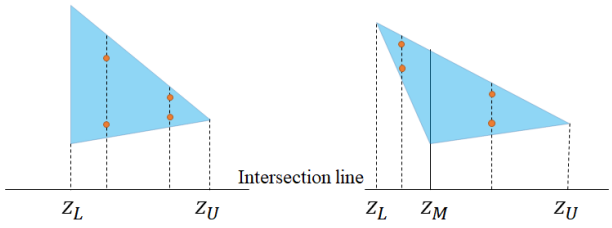

Fig. 3. Geometry for integrating using intersection line; left: no triangle splitting, right: splitting the triangle according to its vertex projections.

III. Analytical Radial Integrals

If we define $\mathbf{r}_i^e$ and $\mathbf{r}_j^f$ as the i-th vertex of test volume element e and the j-th vertex of source volume f, we can write the (unnormalized) SWG test and basis functions [17] as

$$\begin{aligned} \boldsymbol{\Lambda}_i^e(\mathbf{r}) &= \mathbf{r} - \mathbf{r}_i^e = \mathbf{r}'_{S'} - \mathbf{r}_i^e + R_{S'} \hat{\mathbf{R}} \\ \boldsymbol{\Lambda}_j^f(\mathbf{r}') &= \mathbf{r}' - \mathbf{r}_j^f = \mathbf{r}'_{S'} - \mathbf{r}_j^f + R_{S'} \hat{\mathbf{R}} + R' \hat{\mathbf{R}}', \end{aligned} \tag{10}$$

respectively. For the homogeneous medium Green's function, the radial vector potential integrals are thus

$$\begin{aligned} &\int_0^R \int_0^{R_{S'}} \boldsymbol{\Lambda}_i^e(\mathbf{r}) \cdot \boldsymbol{\Lambda}_j^f(\mathbf{r}') \frac{e^{-jkR'}}{4\pi R'} R'^2 dR'\, dR_{S'} \\ &= \frac{1}{4\pi} \int_0^R \int_0^{R_{S'}} P_3(R_{S'}, R')\, e^{-jkR'}\, dR'\, dR_{S'}, \end{aligned} \tag{11}$$

where $P_3(R_{S'}, R') = R' \boldsymbol{\Lambda}_i^e(\mathbf{r}) \cdot \boldsymbol{\Lambda}_j^f(\mathbf{r}')$ is the bivariate cubic polynomial

$$P_3(R_{S'}, R') = R' \left[A + B R_{S'} + R_{S'}^2 + (C - R_{S'}) R' \right], \tag{12}$$

with

$$\begin{aligned} A &= (\mathbf{r}'_{S'} - \mathbf{r}^e_i)\cdot(\mathbf{r}'_{S'} - \mathbf{r}^f_j), \\ B &= \hat{\mathbf{R}}\cdot(2\,\mathbf{r}'_{S'} - \mathbf{r}^f_j - \mathbf{r}^e_i), \\ C &= \hat{\mathbf{R}}'\cdot(\mathbf{r}'_{S'} - \mathbf{r}^e_i). \end{aligned} \tag{13}$$

Integrals of polynomial and exponential products, such as appear in (11), are easily evaluated, but the resulting expressions quickly become unwieldy with increasing polynomial order. A more compact representation for such integrals makes use of exponential integrals of negative order. The following definitions, recursion formulas, and identities, respectively, are needed:

$$\begin{aligned} \int z^n e^{-tz} dz &= -z^{n+1} E_{-n}(tz), \\ E_{-n-1}(z) &= \frac{e^{-z} + (n+1)E_{-n}(z)}{z}, \\ \int z^\ell E_{-n}(tz)\, dz &= \frac{z^{\ell+1}}{\ell - n}\left(E_{-n}(tz) - E_{-\ell}(tz)\right). \end{aligned} \tag{14}$$

The first line of (14) simply notes that the indefinite integral of $z^n e^{-tz}$ can be compactly written in terms of the exponential integral function of negative order n, $E_{-n}(z)$. The recursion formula of the second line allows one to generate exponential integral functions of any negative order from $E_0(z) = \exp(-z)/z$, which result follows either from the defining integral or from setting $n = -1$ in the recursion formula. It is also convenient to define the definite integral,

$$\begin{aligned} \Delta E_{n,\ell}(tR) &= \int_0^R R^\ell\, E_{-n}(tR)\, dR \\ &= \frac{1}{\ell - n}\left(R^{\ell+1}E_{-n}(tR) - R^{\ell+1}E_{-\ell}(tR) + \frac{\ell!}{t^{\ell+1}}\right), \end{aligned} \tag{15}$$

where $\ell > n$, and which may be proved using (14). With these results, the radial vector potential integral (11) is straightforwardly evaluated in closed form as

$$\begin{aligned} &\int_0^R \int_0^{R_{S'}} P_3(R_{S'}, R')\, e^{-jkR'}\, dR'\, dR_{S'} \\ &= A\frac{R - (jk)^2\Delta E_{1,2}(jkR)}{(jk)^2} \\ &+ B\frac{\frac{1}{2}R^2 - (jk)^2\Delta E_{1,3}(jkR)}{(jk)^2} \\ &\quad + \frac{\frac{1}{3}R^3 - (jk)^2\Delta E_{1,4}(jkR)}{(jk)^2} \\ &+ C\frac{2R - (jk)^3\Delta E_{2,3}(jkR)}{(jk)^3} \\ &\quad - \frac{R^2 - (jk)^3\Delta E_{2,4}(jkR)}{(jk)^3}. \end{aligned} \tag{16}$$

To obtain the corresponding static result, we merely set $k = \omega\sqrt{\mu\varepsilon} = 0$ in the integral in (16) and evaluate it directly as

$$\begin{aligned} &\int_0^R \int_0^{R_{S'}} P_3(R_{S'}, R')\; dR'\, dR_{S'} \\ &\qquad = R^3\left[\tfrac{A}{6} + \left(\tfrac{B}{8} + \tfrac{C}{12}\right)R + \tfrac{1}{30}R^2\right]. \end{aligned} \tag{17}$$

The radial *scalar* potential integral corresponding to the *vector* potential integral (11) is similar, but with a product of the (constant) divergences of the vector bases replacing the dot product of bases in (11). Taking the constant as unity, we simply find $P_3 = R'$ replacing (12) in the scalar potential version of (11). I.e., we obtain the scalar potential integrand by dropping all terms on the right hand side of (12) except for the term with coefficient A, which, for this case, we set to unity; doing the same in the right hand sides of (16) or (17) yields the corresponding radial integrals for the dynamic or static scalar potentials, respectively.

IV. Semi-Analytical Static Surface Integrals

To improve efficiency in evaluating the surface integrals (8), we first consider in detail the static case, evaluating analytically the four inner integrals in $(\rho, \rho', R', R_{S'})$, and leaving only the two outer integrals over (z, z') as a 2-D numerical integration over rectangular domains. Here, the kernel function of the radial integral (5) is the static form of the scalar potential multiplied by constant unit basis functions:

$$\begin{aligned} \mathcal{F}(z, \rho, z', \rho') &= -\frac{\rho\rho'\sin^2\beta}{R^4}\int_0^R\int_0^{R_{S'}} \frac{R'^2}{4\pi R'}\, dR'\, dR_{S'} \\ &= -\frac{\rho\rho'\sin^2\beta}{24\pi R}. \end{aligned} \tag{18}$$

Wolfram Mathematica [27] is able to aid in evaluating the integrals over ρ and ρ' if we first make the change of variables

$$\begin{aligned} \rho &= \frac{u' + v'}{\sqrt{2}}, \quad \text{with } u' = \frac{\rho + \rho'}{\sqrt{2}}, \\ \rho' &= \frac{u' - v'}{\sqrt{2}}, \quad \text{with } v' = \frac{\rho - \rho'}{\sqrt{2}}, \end{aligned} \tag{19}$$

and

$$\begin{aligned} u &= u'\sqrt{1 - \cos\beta} = u'\sqrt{2}\sin(\beta/2), \\ v &= v'\sqrt{1 + \cos\beta} = u'\sqrt{2}\cos(\beta/2), \end{aligned} \tag{20}$$

thus eliminating the product term $\rho\rho'$ appearing in (9), and simplifying R to

$$R = \sqrt{u^2 + v^2 + \Delta z^2}. \tag{21}$$

We note that a similar transformation has been used in [28] to evaluate the 4-D potential interaction integrals between triangular element pairs. With this transformation, (18) becomes

$$\begin{aligned} \mathcal{F}(\mathbf{r}, \mathbf{r}') &= -\frac{(u'^2 - v'^2)\sin^2\beta}{48\pi R} \\ &= -\frac{u^2(1 + \cos\beta) - v^2(1 - \cos\beta)}{48\pi\sqrt{u^2 + v^2 + \Delta z^2}}. \end{aligned} \tag{22}$$

Substituting (22) into (8), we then obtain

$$\begin{aligned} I_{\Delta S, \Delta S'} &= -\frac{1}{48\pi|\sin\beta|}\int_{z_L}^{z_U}\int_{z'_L}^{z'_U}\Bigg[(1 + \cos\beta)\int_{D_{uv}} \frac{u^2}{R} du dv \\ &\qquad - (1 - \cos\beta)\int_{D_{uv}} \frac{v^2}{R} du dv\Bigg] dz' dz, \end{aligned} \tag{23}$$

where D_{uv} is the transformed domain of integration shown in Fig. 4. The inner integrals in u and v can be symbolically integrated with the help of Mathematica. It appears that the

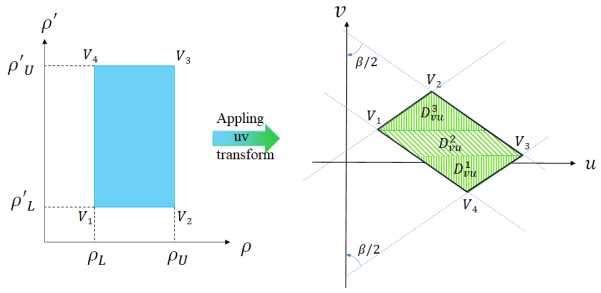

Fig. 4. Domain of integration for ρ-ρ' integrals and the equivalent domain for the u-v transform.

remaining integrals on z and z' must be done numerically, but the above analysis allows us to identify transformations that accelerate the numerical integration of face-pair surface integrals (as detailed in Sect. V).

Note that the two inner double integrals over u and v in (23) are essentially equivalent in the sense that the second can be obtained from the first merely by interchanging the symbols u and v, the order of integration, and the limit parameters. Hence, we consider in detail only the first of the two integrals:

$$\int_{D_{uv}} \frac{u^2}{R} du dv = \frac{1}{2}\int_{v_L}^{v_U} \left[u\,R - \left(\Delta z^2 + v^2\right) \sinh^{-1}\left(\frac{u}{\sqrt{v^2+\Delta z^2}}\right)\right]_{u_L(v)}^{u_U(v)} dv. \tag{24}$$

As shown in Fig. 4, the transformed domain is a parallelogram tilted with respect to the u- and v-axes. If we number the vertex of the original domain ρ-ρ' as indicated in Fig. (4), the vertexes can be described as

$$\begin{aligned} V_1(\rho,\rho') &= (\rho_L, \rho'_L),\\ V_2(\rho,\rho') &= (\rho_U, \rho'_L),\\ V_3(\rho,\rho') &= (\rho_U, \rho'_U),\\ V_4(\rho,\rho') &= (\rho_L, \rho'_U), \end{aligned} \tag{25}$$

and are mapped into the u-v domain as

$$\begin{aligned} V_1(u,v) &= ((\rho_L+\rho'_L)\sin\beta/2, (\rho_L-\rho'_L)\cos\beta/2),\\ V_2(u,v) &= ((\rho_U+\rho'_L)\sin\beta/2, (\rho_U-\rho'_L)\cos\beta/2),\\ V_3(u,v) &= ((\rho_U+\rho'_U)\sin\beta/2, (\rho_U-\rho'_U)\cos\beta/2),\\ V_4(u,v) &= ((\rho_L+\rho'_U)\sin\beta/2, (\rho_L-\rho'_U)\cos\beta/2). \end{aligned} \tag{26}$$

To complete integration of (24), the tilted domain is split into three subdomains, as shown in Fig. 4. The appendix details the definition of these three domains, from which the following integral forms result:

$$\int_{D_{uv}} \frac{u^2}{R} du dv = \frac{1}{2}\sum_{i=1}^{3} I_u^i, \tag{27}$$

where $D_{uv} = \bigcup_{i=1}^{3} D_{uv}^i$ and D_{uv}^i is one of the subdomains into which the tilted rectangle is subdivided. Focusing on one of these three integrals (the other two differing only in their integral limits) we can write,

$$\begin{aligned} I_u^i &= \int_{D_{uv}^i} \frac{u^2}{R} du dv\\ &= \frac{1}{2}\int_{v_L^i}^{v_U^i} \left[uR - \left(\Delta z^2 + v^2\right) \times \sinh^{-1}\left(\frac{u}{\sqrt{v^2+\Delta z^2}}\right)\right]_{u=a_L^i v+b_L^i}^{a_U^i v+b_U^i} dv\\ &= \frac{1}{2}\left[\left[H_{(1)}^i + H_{(2)}^i + H_{(3)}^i\right]_{a=a_L^i, b=b_L^i}^{a_U^i, b_U^i}\right]_{v=v_L^i}^{v_U^i}. \end{aligned} \tag{28}$$

From Mathematica (with $u = av + b$), we find the first term $H_{(1)}^i$ as

$$\begin{aligned} H_{(1)}^i(a,b,v) &= \int (av+b)R dv\\ &= \frac{1}{6}R\left(\frac{a((2a^2+5)b^2+2(a^2+1)\Delta z^2)}{(a^2+1)^2} + \frac{(4a^2+3)bv}{a^2+1} + 2av^2\right)\\ &+ \frac{b\left((a^2+1)\Delta z^2+b^2\right)}{2(a^2+1)^{5/2}} \times \sinh^{-1}\left(\frac{v(a^2+1)+ab}{\sqrt{(a^2+1)\Delta z^2+b^2}}\right), \end{aligned} \tag{29}$$

where R now takes the general form

$$R = \sqrt{(a^2+1)\,v^2 + 2\,a\,b\,v + b^2 + \Delta z^2}. \tag{30}$$

Similarly, for the second integral, $H_{(2)}^i$, we have:

$$\begin{aligned} H_{(2)}^i(a,b,v) &= -\Delta z^2 \int \sinh^{-1}\left(\frac{a\,v+b}{\sqrt{(v^2+\Delta z^2)}}\right) dv\\ &= -\Delta z^2 \left\{H_{(2,1)}^i + H_{(2,2)}^i + 2\,\mathrm{Re}\left[H_{(2,3)}^i\right]\right\}, \end{aligned} \tag{31}$$

where

$$\begin{aligned} H_{(2,1)}^i &= v\sinh^{-1}\left(\frac{a\,v+b}{\sqrt{v^2+\Delta z^2}}\right),\\ H_{(2,2)}^i &= \frac{b}{\sqrt{a^2+1}}\sinh^{-1}\left(\frac{v\,(a^2+1)+a\,b}{\sqrt{(a^2+1)\,\Delta z^2+b^2}}\right),\\ H_{(2,3)}^i &= \frac{j\,\Delta z}{2}\log\left(B(v)\right), \end{aligned} \tag{32}$$

with

$$B(v) = \frac{Cv + D(v)}{v+E}, \tag{33}$$

and where

$$\begin{aligned} C &= (a^2+1)\Delta z + jab,\\ D(v) &= R(a\Delta z + jb) + j(b^2+\Delta z^2) + ab\Delta z.\\ E &= j\Delta z. \end{aligned} \tag{34}$$

In principle, (31) can be verified by direct differentiation.

Writing the complex number B in polar form in (32), we find

$$2\,\mathrm{Re}(H^i_{(2,3)}) = -\Delta z \tan^{-1}\left(\frac{\mathrm{Im}\,(B(v))}{\mathrm{Re}\,(B(v))}\right) = -\Delta z \tan^{-1}\left(\frac{v^2\mathrm{Im}\,C+v\mathrm{Im}(D(v)+CE^*)+\mathrm{Im}(D(v)E^*)}{v^2\mathrm{Re}\,C+v\mathrm{Re}(D(v)+CE^*)+\mathrm{Re}(D(v)E^*)}\right). \quad (35)$$

It is important to note that in evaluating (28) it is not sufficient to merely substitute in the limits v^i_L and v^i_U at the path endpoints on the RHS; we must also ensure that we remain on the same branch of the logarithm function in (32) as v varies from v^i_L to v^i_U. I.e., if $B(v)$ crosses the branch cut along the negative imaginary axis in the complex B-plane as v varies along the integration path, we must account for a jump of $\pm 2\pi j$ in the value of $\log B(v)$ that occurs there. We employed a rudimentary scheme for this: In particular, $B(v)$ is sampled along the path, and if for two adjacent sample points, v_1 and v_2, $\mathrm{Re}\,B(v_1)$ and $\mathrm{Re}\,B(v_2)$ are both negative while $\mathrm{Im}\,B(v_1) \gtrless 0$ and $\mathrm{Im}\,B(v_2) \lesseqgtr 0$, then we add $\pm 2\pi j$ to the value of the arctangent in (35). We also note that R in (34) is not constant, but varies with v, and the factor of the form $\tan^{-1}(y/x)$ in (35) should be evaluated using atan2$\,(y,x)$.

For the third integral, $H^i_{(3)}$, we have

$$H^i_{(3)}(a,b,v) = -\int v^2 \sinh^{-1}\left(\frac{a\,v+b}{\sqrt{v^2+\Delta z^2}}\right) dv = -\frac{1}{6}\Big\{H^i_{(3,1)} + H^i_{(3,2)} + H^i_{(3,3)} + 2\,\mathrm{Re}\left[H^i_{(3,4)}\right]\Big\}, \quad (36)$$

where

$$H^i_{(3,1)} = 2v^3 \sinh^{-1}\left(\frac{a\,v+b}{\sqrt{v^2+\Delta z^2}}\right), \quad (37)$$

$$H^i_{(3,2)} = \frac{R\left(-2a^3\,\Delta z^2 + a^2\,b\,v - 3\,a\,b^2 - 2\,a\,\Delta z^2 + b\,v\right)}{\left(a^2+1\right)^2}, \quad (38)$$

$$H^i_{(3,3)} = \frac{(2a^2-1)b^3 - 3(a^2+1)b\,\Delta z^2}{(a^2+1)^{5/2}} \times \sinh^{-1}\left(\frac{v\,\left(a^2+1\right)+a\,b}{\sqrt{(a^2+1)\,\Delta z^2+b^2}}\right), \quad (39)$$

$$H^i_{(3,4)} = -j\Delta z^3 \log\left(\frac{3}{\Delta z^2}B\right). \quad (40)$$

Again, $2\,\mathrm{Re}(H^i_{(3,4)})$ can be written as

$$2\,\mathrm{Re}(H^i_{(3,4)}) = 2\Delta z^3 \tan^{-1}\left(\frac{\mathrm{Im}(B(v))}{\mathrm{Re}(B(v))}\right) = 2\Delta z^3 \tan^{-1}\left(\frac{v^2\mathrm{Im}\,C+v\mathrm{Im}(D(v)+CE^*)+\mathrm{Im}(D(v)E^*)}{v^2\mathrm{Re}\,C+v\mathrm{Re}(D(v)+CE^*)+\mathrm{Re}(D(v)E^*)}\right), \quad (41)$$

where, as in (35), branch crossings of the argument of the arctangent must be accounted for.

Turning finally to the second inner integral in (23),

$$\int_{D_{uv}} \frac{v^2}{R}\,dudv = \frac{1}{2}\sum_{i=1}^{3} I^i_v, \quad (42)$$

we note it has the same form as I^i_u, but with u and v interchanged and with the limit descriptors a and b replaced by c and d as described in the Appendix. Thus we write I^i_v as

$$I^i_v = \int_{D^i_{uv}} \frac{v^2}{R}\,dvdu = \frac{1}{2}\left[\left[H^i_{(1)} + H^i_{(2)} + H^i_{(3)}\right]^{c^i_U, d^i_U}_{c=c^i_L, d=d^i_L}\right]^{u^i_U}_{u=u^i_L}. \quad (43)$$

Using (27) and (42) we may now write (23) as

$$I_{\Delta S,\Delta S'} = -\frac{1}{48\pi|\sin\beta|}\int_{z_L}^{z_U}\int_{z'_L}^{z'_U}\left[\frac{(1+\cos\beta)}{2}\sum_{i=1}^{3} I^i_u - \frac{(1-\cos\beta)}{2}\sum_{i=1}^{3} I^i_v\right]dz'dz. \quad (44)$$

The remaining integrations over z and z' in (44) are evaluated numerically using GL rules.

V. Acceleration of the Dynamic Surface Integrals

The static kernel results of the previous section can be used to accelerate evaluation of the dynamic potentials by applying the well-known method of singularity subtraction [29]. The integrals can be expressed as a sum of two integrals, first a smoothed-kernel difference term, in which the dominant singular term is removed, plus a separately evaluated (semi-analytic) term representing the singularity's contribution to the integral,

$$I_{V,V'} = \oint_S \oint_{S'} \frac{(\hat{\mathbf{n}}\cdot\hat{\mathbf{R}})(\hat{\mathbf{n}}'\cdot\hat{\mathbf{R}}')}{R^2} \times \int_0^R \int_0^{R_{S'}} F(\mathbf{r},\mathbf{r}')R'^2 dR' dR_{S'} dS' dS = I_{\text{num}} + I_{\text{sa}}, \quad (45)$$

where I_{sa} is the semi-analytical evaluation of integral (23), and

$$I_{\text{num}} = \int_z\int_{z'}\int_\rho\int_{\rho'} \frac{(\hat{\mathbf{n}}\cdot\hat{\mathbf{R}})(\hat{\mathbf{n}}'\cdot\hat{\mathbf{R}}')}{R^2} I_{\text{R\_num}}\,d\rho'\,d\rho\,dz'dz, \quad (46)$$

with

$$I_{\text{R\_num}} = \int_0^R \int_0^{R_{S'}} \frac{\mathbf{\Lambda}^e_i(\mathbf{r})\cdot\mathbf{\Lambda}^f_j(\mathbf{r}')e^{-jkR'} - A}{4\pi R'} R'^2 dR' dR_{S'}, \quad (47)$$

and where $A = \lim_{R'\to 0} \mathbf{\Lambda}^e_i(\mathbf{r})\cdot\mathbf{\Lambda}^f_j(\mathbf{r}')$ is defined in (13). The integral (47) can be evaluated analytically using the procedure of Sect. III.

VI. Numerical Results

In this section, we examine the convergence characteristics of both triangular face-pair and tetrahedral element-pair interaction integrals that occur in volumetric integral equation (VIE) modeling. We assess the accuracy and convergence of a computed integral by reporting the number of correct significant digits (SD),

$$\mathrm{SD} = -\log_{10}\left(\left|\frac{I^{\mathrm{ref}} - I^N}{I^{\mathrm{ref}}}\right| + \delta\right), \tag{48}$$

where I^N is the computed integral value using N sample points and I^{ref} is the associated reference value. Reference values are obtained using the highest order quadrature scheme available for each case; they are computed in quad precision and checked for convergence to at least 16 significant digits. Adding the term $\delta = 10^{-16}$ to the argument of the logarithm in (48) limits quoted precision to no more than 16 digits (double precision). If an integral is the sum of two computed integrals, $I_1^{N_1}$ and $I_2^{N_2}$, using N_1 and N_2 sample points, respectively, (as in (45)), it is convenient to be able to independently assess the convergence of each partial contribution by reporting

$$\mathrm{SD}_i = -\log_{10}\left(\left|\frac{I_i^{\mathrm{ref}} - I_i^{N_i}}{I^{\mathrm{ref}}}\right| + \delta\right), \quad i = 1, 2. \tag{49}$$

Note that the normalization for each integral is with respect to the reference value of the *total* integral, $I^{\mathrm{ref}} = I_1^{\mathrm{ref}} + I_2^{\mathrm{ref}}$, ensuring that SD for the total satisfies $\mathrm{SD} \geq \min(\mathrm{SD}_1, \mathrm{SD}_2) - \log_{10}(2)$, i.e., one can say that, to within less than a third of a significant digit, the inequality $\mathrm{SD} \geq \min(\mathrm{SD}_1, \mathrm{SD}_2)$ holds. This further suggests that choosing N_1 and N_2 such that $\mathrm{SD}_1 \approx \mathrm{SD}_2$ is nearly optimal in terms of minimizing the number of sample points for a given SD requirement.

Two quadrature schemes, either an outer product of two 1-D Gauss-Legendre (GL) rules or a Gauss-over-triangle (GT) rule are used to numerically evaluate all surface (face) integrals. Plots of SD convergence are with respect to n, the (geometric) *average number of quadrature points per dimension*. I.e., if a numerically evaluated integral is evaluated using a total of N sample points over d dimensions, $n = N^{1/d}$ is the number of points along each edge of the uniformly sampled d-dimensional hypercube. Thus, for fully volumetric numerical integration over source and testing tetrahedral pairs (six integration dimensions), the total number of sample points would be n^6 points, whereas for integration over face pairs or over a tetrahedral pair reduced to surface integrals only (four integration dimensions), the total number of sample points is n^4 points. For a sum I_1+I_2 of integrals of different quadrature dimensionalities, say I_1 a d_1-dimensional integral of n_1 and I_2 a d_2-dimensional integral of n_2 average points per dimension, the total number of points required is therefore $n_1^{d_1} + n_2^{d_2}$, with the average point density per dimension determined as $(n_1^{d_1}+n_2^{d_2})^{1/d_2}$, assuming $d_2 \geq d_1$. Reported this way, integrals with *smooth* integrands should asymptotically exhibit exponential convergence, i.e., SD should (asymptotically) converge linearly with respect to the average number of sample points per dimension.

A. Face-Pair Interactions

Since volume interaction integrals are numerically evaluated as surface integral sums over face-pairs, the convergence rate of the interaction integral (3) for a tetrahedral pair is limited by the slowest converging of its face-pair integrals. Hence, it is useful to first simply consider the evaluation of interaction integrals between variously configured face pairs alone. Hence we examine the convergence of (4) for the following three possible face-pair configurations: a pair of non-touching faces, a pair with a common vertex, and a pair sharing a common edge, as illustrated by the row of figures near the top of Table I. For all examples, triangle face edge lengths are around 0.1λ, and the basis functions are (unnormalized) SWG bases [17]. Each triangular face contains only three of the four vertices defining the four SWG bases associated with a tetrahedron. The fourth, however, can be written as a linear combination of the other three; hence it suffices to consider just the nine SWG basis and *vector* potential combinations associated with the vertices of the source and test face pair. Since each basis has a constant divergence, only a single independent *scalar* potential is associated with a face-pair, however, and computations show that the nine *vector* potential integrals differ from the single scalar potential integral by no more than one or two significant digits. Hence it also suffices to show only scalar potential integral convergence.

Figures 5a, 6a, and 7a show convergence for a non-touching, a common-vertex, and a common-edge source and test face pair, respectively. In all three cases, the radial integrals are evaluated analytically, and the following five scalar potential face-pair surface integral approaches are examined:

- "S-S'": direct integration of (4) using GT quadrature for both source and test face (4-D) integrals with no acceleration.
- "(z,ρ)-(z',ρ')": direct integration of (8) using outer products of GL rules for both the (ρ,ρ') and the (z,z') (4-D) integrals with no acceleration.
- "(z,ρ)-(z',ρ') difference": same as above, but integrating the difference integral, (46) and (47), resulting from removing the most singular (static) part of the integrand.
- "Semi-Analytical": the semi-analytical integral (23) representing the removed dominant singularity integrand contribution of the case above. The (ρ,ρ') (2-D) integration is performed analytically; the remaining z-z' integral is performed by GL quadrature.
- "Difference + Semi-Analytical": accelerated form of the integral (4) expressed as the sum of the semi-analytical (2-D) integral plus the (z,ρ)-(z',ρ') (4-D) difference integral as in (45).

We note in Fig. 5a the near-linear asymptotic convergence to full precision. All integrals there also exhibit similar convergence rates with respect to sampling density. By contrast, in Figs. 6a and 7a, in which the face pairs share a vertex or an edge, respectively, convergence rates are not only reduced, but, except for the difference integral, appear to stagnate with increasing sample density, strongly suggesting the presence of a low order singularity (e.g., a singular *derivative*) in the integrand. However, the accelerated form (difference plus

TABLE I
FACE PAIR INTERACTION TYPES FOR A TETRAHEDRAL ELEMENT PAIR

	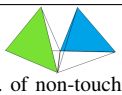 No. of non-touching face pairs	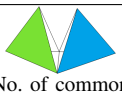 No. of common vertex face pairs	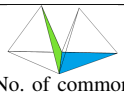 No. of common edge face pairs	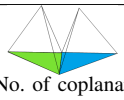 No. of coplanar face pairs
Non-touching 	16,15,14,13	0	0	0,1,2,3
Common vertex 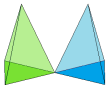	7	9,8,7,6	0	0,1,2,3
Common edge 	2	10,9	4,3,2	0,1,2,3
Common face 	0	6	9,8,7	1,2,3
Self-term 	0	0	12	4

semi-analytical integral) exhibits faster convergence in the low-to-medium sampling density range, and for the common vertex case of Fig. 6a, is able to reach machine precision needing only a few more sampling points than the non-touching case. For the common edge case of Fig. 7a, however, convergence of the total integral is severely limited by the semi-analytical integral, which is only able to reach 10 SD. It seems reasonable to expect that proper handling of low order singularities in the semi-analytical integral would improve the convergence of cases involving vertex sharing, allowing one to reach machine precision in these cases as well.

Figures 5b, 6b, and 7b show the corresponding computation times needed to compute the integrals versus the SD accuracy achieved. The reported times are normalized with respect to the time required to compute the (unaccelerated) surface-surface or (S-S') integral using $\sqrt{166}$ integration points per linear dimension. Both quantities in the ratio are computed twenty times to average out small CPU time fluctuations. The total time needed to evaluate the integral (3) using the acceleration method of Sect. V is the sum of the CPU times needed for the (z,ρ)-(z',ρ') difference integral plus that needed for the z-z' semi-analytical integral. With logarithmic time axes, the total CPU time reported appears only slightly larger than the slower of the two, as seen in Figs. 5b, 6b, and 7b. It appears that CPU times would also benefit from improving the convergence of the semi-analytical integral for face pairs sharing one or more vertices.

The contour plots in Fig. 8 show the number of correct SD for the scalar potential of a common-edge face pair for a fixed equilateral source face whose common edge length is $\lambda/10$ and for different-shaped test faces. We examine only the common-edge interaction case since that case exhibits the poorest convergence, as previously noted. It is assumed that the common edge of length $\lambda/10$ is also the longest edge of the test triangle, and the two remaining edges are allowed to assume all possible lengths $\leq \lambda/10$. Thus the third vertex of the test triangle is limited to the region bounded by circular arcs of radii $\lambda/10$ centered on the vertices of the common edge as shown in Fig. 8(a). If the third vertex, assumed to be at point (x,y), falls at the intersection of the arcs, then both the source *and* the test triangle are equilateral. Since the computations are symmetric about the line from the midpoint of the common edge to the intersection of the circular arcs, Figs. 8 (b) and (c) show only one-half the region bounded by the circular arcs. The color at each point (x,y) of the figure represents the number of correct SD in the tested potential integral for a test triangle with its third vertex located at that point. For all integrals, the GL scheme with 5 points per linear dimension is used. In Fig. 8(b), the "(z,ρ)-(z',ρ')" approach is applied, whereas in Fig. 8(c), the reported results are obtained with the "Difference + Semi-Analytical" method. Figures 8 (b) and (c) illustrate that the "(z,ρ)-(z',ρ')" approach is not particularly sensitive to shape, whereas the "Difference + Semi-Analytical" evaluation provides higher accuracy for a fixed number of sample points without compromising shape insensitivity.

B. *Tetrahedral-Pair Interactions*

Tetrahedral-pair interactions are computed as sums over non-vanishing face-pair interactions. Face pair integrals vanish (hence, need not be evaluated) whenever the faces are coplanar, since then the integrand factor $(\hat{\mathbf{n}}\cdot\hat{\mathbf{R}})(\hat{\mathbf{n}}'\cdot\hat{\mathbf{R}}')$ vanishes identically.

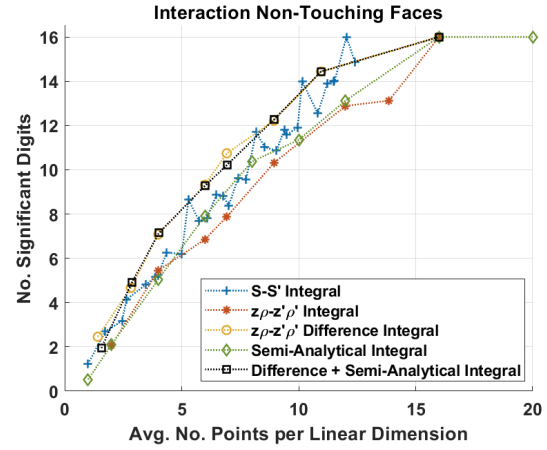

(a)

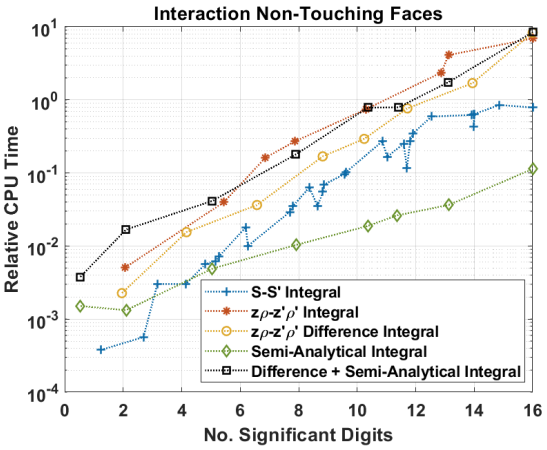

(b)

Fig. 5. Convergence rates of proposed methods for a pair of nearby but non-touching faces. (a) Number of correct SD versus the average number of points per linear dimension; the total number of points is the fourth power of the number of points per linear dimension; and (b) normalized CPU time versus number of correct SD.

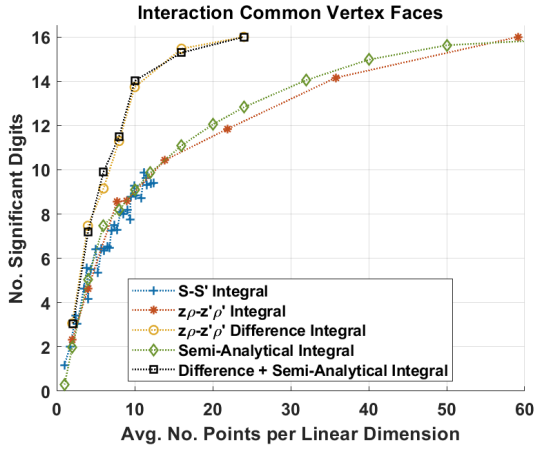

(a)

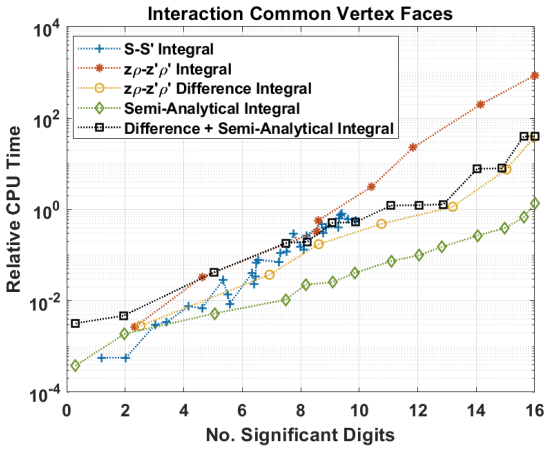

(b)

Fig. 6. Convergence rates of proposed methods for a pair of common vertex faces. (a) Number of correct SD versus the average number of points per linear dimension; the total number of points is the fourth power of the number of points per linear dimension; and (b) normalized CPU time versus number of correct SD.

The total number of sample points for the integral (3) over a tetrahedral element pair, evaluated as a sum of surface integrals over their faces, may be estimated as $n^4 N_{\text{comb}}$ where N_{comb} is the number of non-vanishing face pair integral combinations, and n is the number of quadrature points per linear dimension for a face pair. For tetrahedral elements, no more than three face pairs can be coplanar (and hence vanishing), except for self-interaction integrals where four face pairs are coplanar. Therefore, the number of non-vanishing face pair combinations for a pair of interacting tetrahedra can vary between 12 (reduces to 6 if we also account for the face-pair ordering independence property for self-element face interactions) and 16.

The number of possible face-pair combinations for each connectivity type for conformal tetrahedral elements is summarized in Table I. The rows of Table I correspond to different source and test tetrahedron adjacency configurations, while the columns correspond to possible face-pair adjacency configurations; listed for each case is the number of face-pairs of that type possible for the tetrahedral pair. For a given tetrahedral pair configuration, a numerical distribution of face-pair types is possible if it results from selecting a number from each column such that their sum is 16. For example, for a pair of non-touching tetrahedra, no face pairs touch, and so up to $4 \times 4 = 16$ different face pairs integrals can contribute. But up to three face pairs may be coplanar (hence have vanishing integral contributions), so that the number of non-touching face-pair integrals that must be computed is reduced by the same number, as indicated in the "Non-touching" row of Table I. For the "Common edge" configuration, either a common vertex pair and/or up to two common edge pairs may be coplanar and the number of coplanar faces can be up to three.

Figures 9–13 examine convergence for a pair of non-touching tetrahedra, as well as for a pair with a common vertex, a common edge, a common face, and the self-term case using the proposed methods. For each case, convergence plots are presented for face-pair integration schemes using GT quadrature, dyadic product of GL rules, and the acceleration approach of (45). The labeling for each is the same as for the earlier face-pair analyses. With regard to using these results

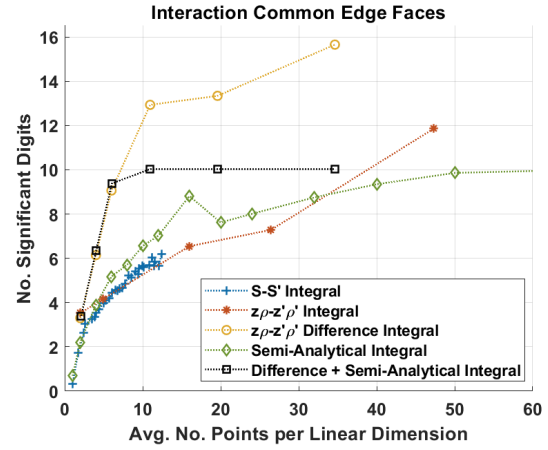

(a)

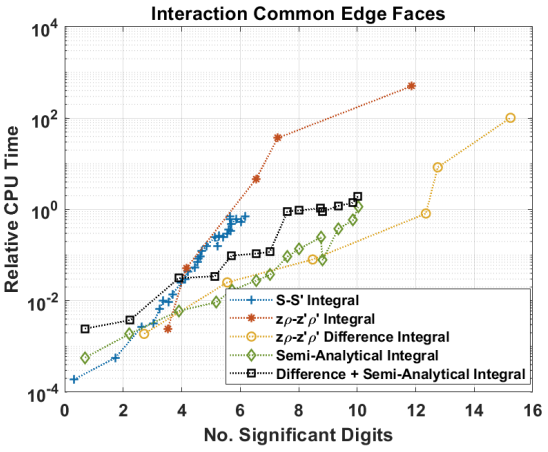

(b)

Fig. 7. Convergence rates of proposed methods for a pair of common edge faces. (a) Number of correct SD versus the average number of points per linear dimension; the total number of points is the fourth power of the number of points per linear dimension; and (b) normalized CPU time versus number of correct SD.

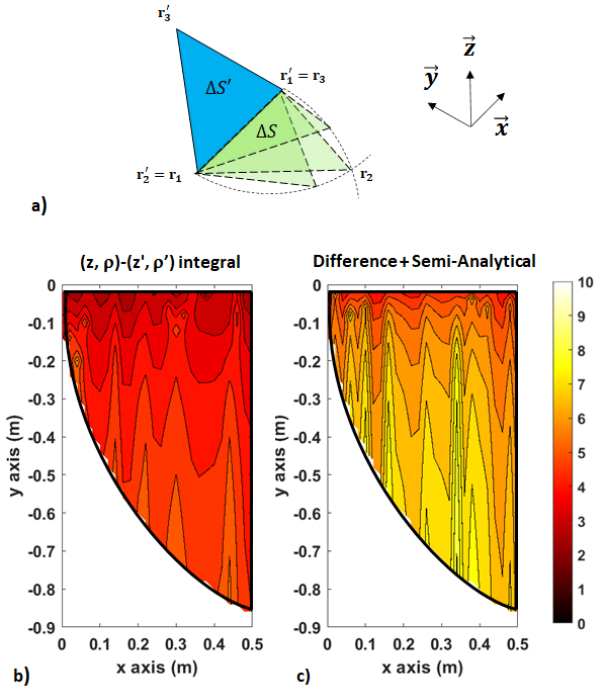

Fig. 8. SD for scalar potential versus triangle shape for an edge-adjacent triangle pair, (a) one a fixed source equilateral triangle with vertices $\mathbf{r}'_1 = (1,0,0)$, $\mathbf{r}'_2 = (0,0,0)$, and $\mathbf{r}'_3 = (1/2, 0, \sqrt{3}/2)$ whose edge lengths are $\lambda/10$, and the second, a test triangle placed in the plane $z = 0$ with vertices at $\mathbf{r}_3 = \mathbf{r}'_1$ and $\mathbf{r}_1 = \mathbf{r}'_2$. The color at any point (x, y) locating vertex $\mathbf{r}_2$ is keyed to the colorbar which indicates the number of correct SD for that triangle shape with (b) the "(z, ρ)-(z', ρ')" approach and (c) the "Difference + Semi-Analytical" method applied. The number of sample points per linear dimension is fixed at 5 (GL quadrature rule). The plots are symmetric and only the left half of each is shown.

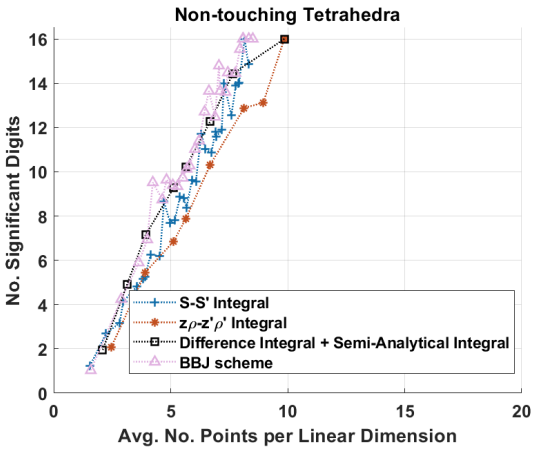

Fig. 9. Convergence rate for a pair of non-touching tetrahedra for various methods versus the average number of points per linear dimension. The total number of points is the sixth power of the number of points per linear dimension. Also shown (label "BBJ") is the approach of [16] .

in VIE MoM formulations, note that we are not including scalar potential surface integral contributions that arise due to material boundary discontinuities.

All the figures include for comparison the (unaccelerated) approach of [16], labelled as "BBJ scheme". The two formulations share the goal of reducing volumetric integrals to surface integrals, but differ in several other important aspects. In [16], for example, one first determines an auxiliary function whose Laplacian yields the Green's function; finding the inverse Laplacian is equivalent to integrating twice in the radial variable. But in our approach, the product of basis, test, and Green's functions are altogether integrated twice in the radial variable. Both methods contain dot product factors that appear in the integrand of the outer surface integrals, but they take quite different forms: $(\hat{\mathbf{n}} \cdot \hat{\mathbf{n}}')$ in the approach of [16], as compared to $(\hat{\mathbf{n}} \cdot \hat{\mathbf{R}})(\hat{\mathbf{n}}' \cdot \hat{\mathbf{R}}')/R^2$ for our approach. At first glance, it may appear that the latter is not only rapidly varying, but indeed, singular as $R \to 0$. A more careful examination reveals, however, that the two terms cannot be considered alone, but rather must incorporate the behavior of the radial integral factors in the integrands, which introduce multiplicative terms of order $O(R)$ and $O(R^3)$, respectively. With this observation, we find the integrands of both approaches not only remain bounded, but both actually *vanish* as $R \to 0$. There is one striking difference between the two approaches, however; in the approach of [16], the dot product factor always vanishes

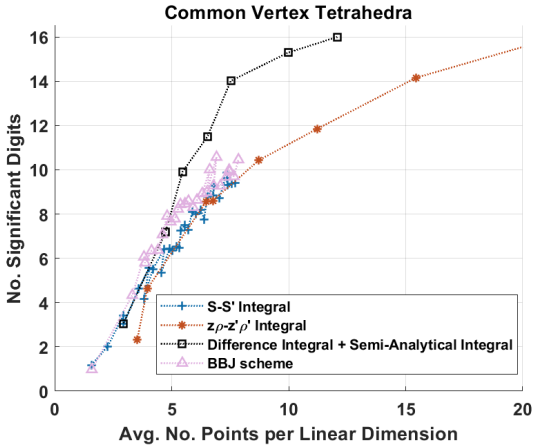

Fig. 10. Convergence rate for a pair of common vertex tetrahedra for various methods versus the average number of points per linear dimension. The total number of points is the sixth power of the number of points per linear dimension. Also shown (label "BBJ") is the approach of [16].

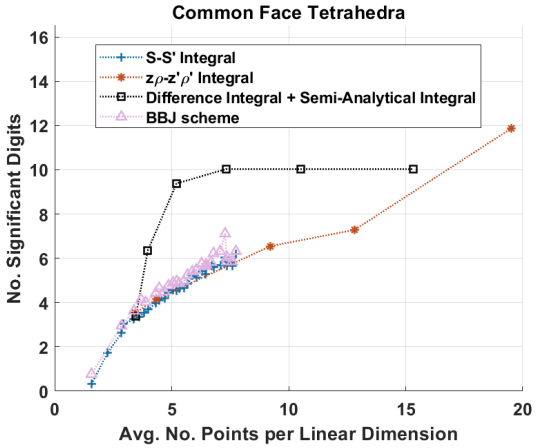

Fig. 12. Convergence rate for a pair of common face tetrahedra for various methods versus the average number of points per linear dimension. The total number of points is the sixth power of the number of points per linear dimension. Also shown (label "BBJ") is the approach of [16] .

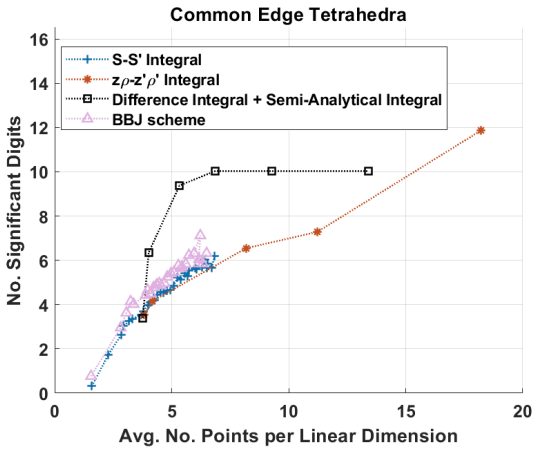

Fig. 11. Convergence rate for a pair of common edge tetrahedra for various methods versus the average number of points per linear dimension. The total number of points is the sixth power of the number of points per linear dimension. Also shown (label "BBJ") is the approach of [16].

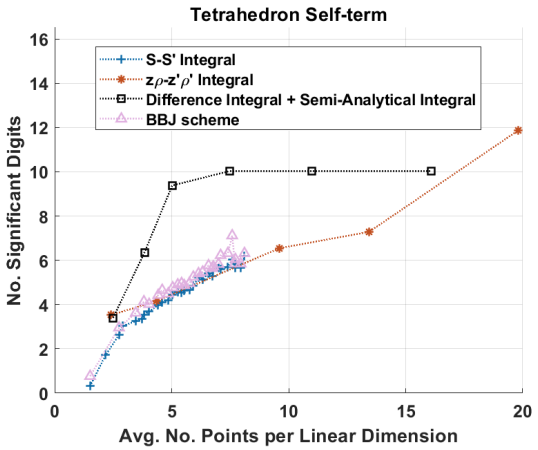

Fig. 13. Convergence rate of a self-term for various methods versus the average number of points per linear dimension. The total number of points is the sixth power of the number of points per linear dimension. Also shown (label "BBJ") is the approach of [16].

for *orthogonal* source and test face pairs, whereas in our approach, the factor vanishes for *coplanar* face pairs. This latter property may be used to considerable advantage to reduce the total effort needed for the all-important self-term calculations, where *every* source face is coincident (and hence coplanar) with its corresponding test face. Interestingly, despite their differences, in their *unaccelerated* forms, both approaches are found to exhibit similar convergence characteristics.

As the figures show, without accelerated convergence, rates are roughly independent of formulation or quadrature scheme chosen, and the more vertices shared by the the two tetrahedrons, the slower the convergence rate. But our approach benefits considerably from the accelerated convergence offered by the simple singularity subtraction scheme of (45); one might expect that the scheme of [16] would similarly benefit from some form of acceleration. Indeed, the departure of Figs. 10–13 from the near-linear convergence of Fig. 9 strongly suggests the presence of at least a low-order singularity in the integrand of both formulations when the source and testing tetrahedra have at least a vertex in common.

Though it is difficult to compare directly with recent results by Reid [19], our results exhibit similar values in terms of number of kernel sample points per dimension, as well as in rates of convergence. The approach of [19] required considerable extra analytical effort as well as automatic code generation, but it does appear capable of achieving full double precision. Further improvement in evaluating the semi-analytical static integral for our case likely would also improve our ability to approach machine precision.

VII. Conclusion and Perspectives

We propose a scheme based on applying the divergence theorem twice along with an appropriate integration reordering. The volume integrals are expressed as two radial integrals plus two surface integrals over source and observation domain boundaries. A closed form evaluation for the radial integrals is

derived for the homogeneous medium kernel and standard linear basis and testing functions. A simple acceleration scheme is developed based on a singularity subtraction approach using a semi-analytic evaluation of the static form of the kernel. The method is numerically validated, both with and without acceleration, for both the vector and scalar potential dynamic kernels arising in the electric field volume integral equations; with no acceleration, convergence is found to be similar to that of comparable existing schemes, but is considerably improved by the simple acceleration scheme. Further improvement may follow if accuracy limitations on computation of the static integral can be removed.

A possible next step is to extend the approach to other singular kernels, particularly to those with $\nabla(1/R)$ singularities. Moreover, the proposed approach likely can be extended to higher-order basis functions and curvilinear tetrahedron elements as treated in [30], [31]. These objectives hopefully will be pursued in future work.

ACKNOWLEDGMENT

The authors would like to thank Dr. J. A. Tobon Vasquez for his assistance in performing the calculations.

APPENDIX

Once the change of variables from ρ-ρ' to u-v is implemented, it is necessary to adapt the limits of integration to a non-rectangular domain of integration split into three parts (see Fig. 4). The new limits of integrations are defined by the geometry of the two faces of the interacting pair, and the angle between them, i.e., they depend on ρ, ρ', and β. Since the domain of integration is a parallelogram, the equation for each edge takes the generic form $u = av + b$, with constants a and b depending on the edge under consideration. For each value of $v_u^i(v_l^i)$, we have a pair of slopes $a_u^i(a_l^i)$ and intercepts, $b_u^i, (b_l^i)$, defining the lines representing integration limits in u. The parallelogram consists on 4 lines: the lines joining the vertexes $\mathbf{V}_2$-$\mathbf{V}_1$, $\mathbf{V}_4$-$\mathbf{V}_3$, $\mathbf{V}_3$-$\mathbf{V}_2$, and $\mathbf{V}_4$-$\mathbf{V}_1$. Each one of the lines can be expressed in slope-intercept form as

$$\begin{aligned}
\mathbf{V}_2\text{-}\mathbf{V}_1 &: \quad u = \tan\frac{\beta}{2}v + 2\rho_l' \sin\frac{\beta}{2} \\
\mathbf{V}_4\text{-}\mathbf{V}_3 &: \quad u = \tan\frac{\beta}{2}v + 2\rho_u' \sin\frac{\beta}{2} \\
\mathbf{V}_3\text{-}\mathbf{V}_2 &: \quad u = -\tan\frac{\beta}{2}v + 2\rho_u \sin\frac{\beta}{2} \\
\mathbf{V}_4\text{-}\mathbf{V}_1 &: \quad u = -\tan\frac{\beta}{2}v + 2\rho_l \sin\frac{\beta}{2}.
\end{aligned} \tag{50}$$

If we consider the integral (27), where we integrated first in u, holding v constant, then integrate on v, as

$$\int_{D_{vu}^i} \frac{u^2}{R}\, dudv \;=\; \int_{v_L^i}^{v_U^i} \int_{u_L^i = a_L^i v + b_L^i}^{u_U^i = a_U^i v + b_U^i} \frac{u^2}{R}\, dudv, \tag{51}$$

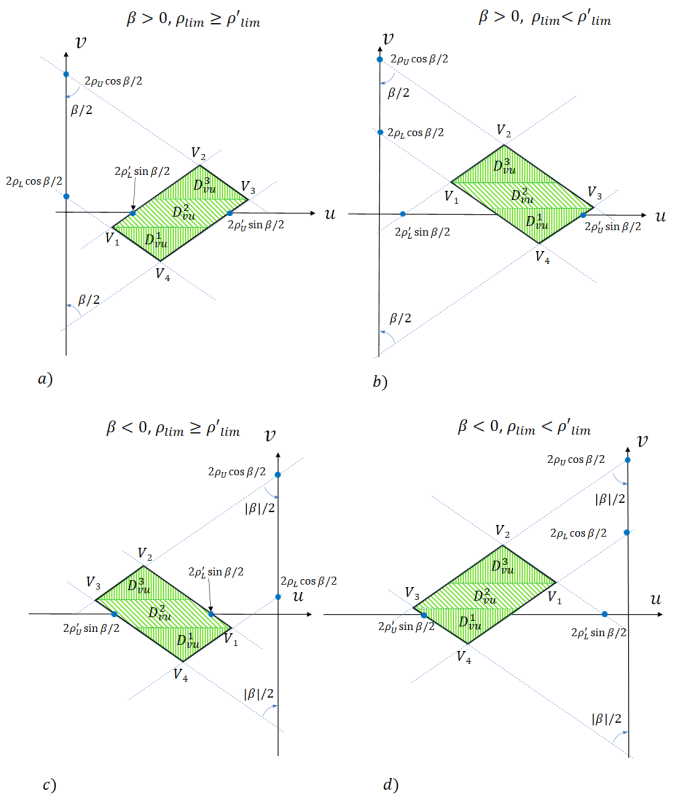

Fig. 14. Different orientation of the domains of integration for u-v integrals; $v_{i,l}$ and $v_{i,u}$ are the lower and upper integration limits of v. Transformation of a rectangular domain in (ρ, ρ') coordinates forms a parallelogram in the (u, v) domain. Note that in (b) the ordering of the v-axis projections of vertices V_1 and V_3, as well as $v_{2,l}$ and $v_{2,u}$, are reversed from that of (a). Subfigures (c) and (d) are the mirrored design of (a) and (b) respectively when $\beta < 0$. In these two last cases the upper and lower limit are the opposite of their equivalents in the case that $\beta > 0$.

then for $\beta > 0$, we can define the limits in v as

$$\begin{aligned}
v_L^1 &= (\rho_L - \rho_U') \cos\frac{\beta}{2}, \\
v_U^1 = v_L^2 &= (\min(\rho_U - \rho_U', \rho_L - \rho_L')) \cos\frac{\beta}{2}, \\
v_U^2 = v_L^3 &= (\max(\rho_U - \rho_U', \rho_L - \rho_L')) \cos\frac{\beta}{2}, \\
v_U^3 &= (\rho_U - \rho_L') \cos\frac{\beta}{2},
\end{aligned} \tag{52}$$

and the limits in u with respect to v as

$$\begin{aligned}
a_L^1 &= -\tan\beta/2, \quad a_U^1 = \tan\beta/2, \\
a_L^2 &= \begin{cases} \tan\beta/2, & \text{if } \rho_{\text{lim}} \geq \rho'_{\text{lim}} \\ -\tan\beta/2, & \text{otherwise} \end{cases} \\
a_U^2 &= \begin{cases} \tan\beta/2, & \text{if } \rho_{\text{lim}} \geq \rho'_{\text{lim}} \\ -\tan\beta/2, & \text{otherwise} \end{cases} \\
a_L^3 &= \tan\beta/2, \quad a_U^3 = -\tan\beta/2,
\end{aligned} \tag{53}$$

and

$$b_L^1 = 2\rho_L \sin\beta/2, \quad b_U^1 = 2\rho'_U \sin\beta/2,$$
$$b_L^2 = \begin{cases} 2\rho'_L \sin\beta/2, & \text{if } \rho_{\text{lim}} \geq \rho'_{\text{lim}} \\ 2\rho_L \sin\beta/2, & \text{otherwise} \end{cases}$$
$$b_U^2 = \begin{cases} 2\rho'_U \sin\beta/2, & \text{if } \rho_{\text{lim}} \geq \rho'_{\text{lim}} \\ 2\rho_U \sin\beta/2, & \text{otherwise} \end{cases}$$
$$b_L^3 = 2\rho'_L \sin\beta/2, \quad b_U^3 = 2\rho_U \sin\beta/2, \tag{54}$$

where $\rho_{\text{lim}} = \rho_U - \rho_L$, and $\rho'_{\text{lim}} = \rho'_U - \rho'_L$. The ambiguities in (53) and (54), arise because the $v-$axis projections of vertices 1 and 3 may switch positions depending on the triangle geometries, as shown in Fig. 14 (*a–b*). On the other hand, if $\beta < 0$, the domain of integration is mirrored with respect to the $v-$axis, as can be seen in Fig. 14 (*c–d*). In this case the definition of the order of integration is interchanged, i.e.,

$$\begin{aligned} a_L^i(\beta > 0) &\Rightarrow a_U^i(\beta < 0) \\ a_U^i(\beta > 0) &\Rightarrow a_L^i(\beta < 0) \\ b_L^i(\beta > 0) &\Rightarrow b_U^i(\beta < 0) \\ b_U^i(\beta > 0) &\Rightarrow b_L^i(\beta < 0), \end{aligned} \tag{55}$$

and a negative sign is included in the integration.

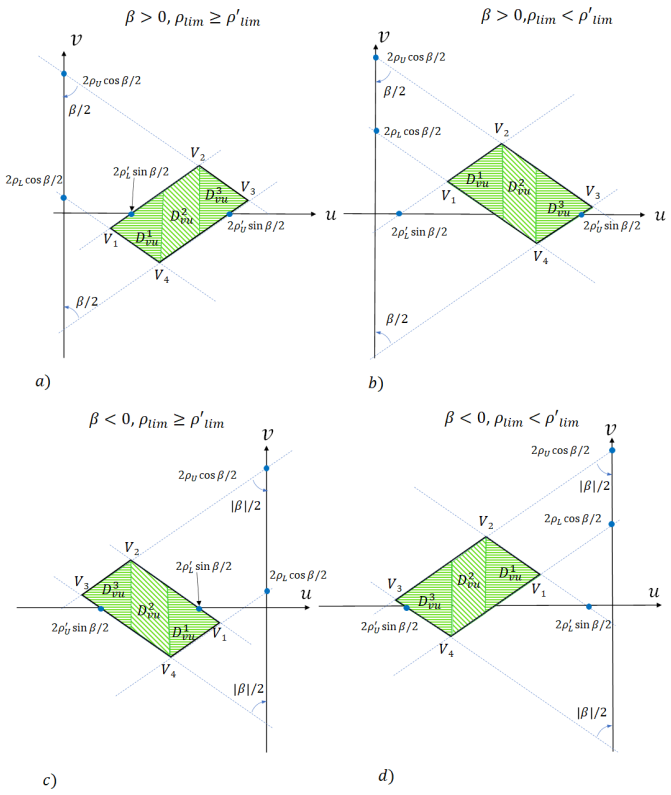

Fig. 15. Different orientation of the domains of integration for v-u integrals; $u_{i,l}$ and $u_{i,u}$ are the lower and upper integration limits of on u. Transformation of a rectangular domain in (ρ, ρ') coordinates forms a parallelogram in the (u, v) domain. Note that in (b) the ordering of the u-axis projections of vertices V_2 and V_4, as well as $u_{2,l}$ and $u_{2,u}$, are reversed from that of (a). Subfigures (c) and (d) are the mirrored design of (a) and (b) respectively when $\beta < 0$. In these two last cases the upper and lower limit are the opposite of their equivalents in the case that $\beta > 0$.

We turn our focus next to the integral (42), where we integrate first in v, holding u constant, then integrate on u, as

$$\int_{D^i_{vu}} \frac{v^2}{R}\, dvdu = \int_{u_L^i}^{u_U^i} \int_{v_L^i = c_L^i u + d_L^i}^{v_U^i = c_U^i u + d_U^i} \frac{v^2}{R}\, dvdu, \tag{56}$$

where the limits in u for $\beta > 0$ are

$$\begin{aligned} u_L^1 &= (\rho_L + \rho'_L)\sin\beta/2, \\ u_U^1 = u_L^2 &= (\min(\rho_U + \rho'_L, \rho_L + \rho'_U))\sin\beta/2, \\ u_U^2 = u_L^3 &= (\max(\rho_U + \rho'_L, \rho_L + \rho'_U))\sin\beta/2, \\ u_U^3 &= (\rho_U + \rho'_U)\sin\beta/2. \end{aligned} \tag{57}$$

In this case, v depends linearly on u as $v = cu + d$, where the slopes and intercepts for the various boundary lines are

$$c_L^1 = -\cot\beta/2, \quad c_U^1 = \cot\beta/2,$$
$$c_L^2 = \begin{cases} \cot\beta/2, & \text{if } \rho_{\text{lim}} \geq \rho'_{\text{lim}} \\ -\cot\beta/2, & \text{otherwise} \end{cases}$$
$$c_U^2 = \begin{cases} \cot\beta/2, & \text{if } \rho_{\text{lim}} \geq \rho'_{\text{lim}} \\ -\cot\beta/2, & \text{otherwise} \end{cases}$$
$$c_L^3 = \cot\beta/2, \quad c_U^3 = -\cot\beta/2, \tag{58}$$

and

$$d_L^1 = 2\rho_L \cos\beta/2, \quad d_U^1 = -2\rho'_L \cos\beta/2,$$
$$d_L^2 = \begin{cases} -2\rho'_U \cos\beta/2, & \text{if } \rho_{\text{lim}} \geq \rho'_{\text{lim}} \\ 2\rho_L \cos\beta/2, & \text{otherwise} \end{cases}$$
$$d_U^2 = \begin{cases} -2\rho'_L \cos\beta/2, & \text{if } \rho_{\text{lim}} \geq \rho'_{\text{lim}} \\ 2\rho_U \cos\beta/2, & \text{otherwise} \end{cases}$$
$$d_L^3 = -2\rho'_U \cos\beta/2, \quad d_U^3 = 2\rho_U \sin\beta/2. \tag{59}$$

Again, the ambiguities in (58) and (59) arise from the two possible positions of the projections vertices 2 and 4, as shown in Fig. 15(*a–b*). And once again, if $\beta < 0$, the domain of integration is mirrored respect to the $v-$axis, as can be seen in Fig. 15 (*c–d*). In this case the definition of the order of integration is interchanged, i.e.,

$$\begin{aligned} c_L^i(\beta > 0) &\Rightarrow c_U^i(\beta < 0) \\ c_U^i(\beta > 0) &\Rightarrow c_L^i(\beta < 0) \\ d_L^i(\beta > 0) &\Rightarrow d_U^i(\beta < 0) \\ d_U^i(\beta > 0) &\Rightarrow d_L^i(\beta < 0), \end{aligned} \tag{60}$$

and a negative sign is included in the integration.

REFERENCES

[1] M. M. Botha, "Solving the volume integral equations of electromagnetic scattering," *Journal of Computational Physics*, vol. 218, no. 1, pp. 141–158, Oct. 2006. [Online]. Available: https://linkinghub.elsevier.com/retrieve/pii/S0021999106000763

[2] M. S. Tong, Z.-G. Qian, and W. C. Chew, "Nyström Method Solution of Volume Integral Equations for Electromagnetic Scattering by 3D Penetrable Objects," *IEEE Transactions on Antennas and Propagation*, vol. 58, no. 5, pp. 1645–1652, May 2010. [Online]. Available: http://ieeexplore.ieee.org/document/5422698/

[3] Y. He, J. F. Li, X. J. Jing, and M. S. Tong, "Fast Solution of Volume–Surface Integral Equations for Multiscale Structures," *IEEE Transactions on Antennas and Propagation*, vol. 67, no. 12, pp. 7649–7654, Dec. 2019. [Online]. Available: https://ieeexplore.ieee.org/document/8852840/

[4] H.-Y. Chen and D.-P. Lin, "Volume integral equation solution of microwave absorption and scattering by raindrops," in *IEEE Antennas and Propagation Society International Symposium. 1999 Digest. Held in conjunction with: USNC/URSI National Radio Science Meeting (Cat. No.99CH37010)*, vol. 4. Orlando, FL, USA: IEEE, 1999, pp. 2676–2679. [Online]. Available: http://ieeexplore.ieee.org/document/789359/

[5] S. Zeng, D. Li, D. R. Wilton, and J. Chen, "Fast and accurate simulation of electromagnetic telemetry in deviated and horizontal drilling," *Journal of Petroleum Science and Engineering*, vol. 166, pp. 242–248, Jul. 2018. [Online]. Available: http://www.sciencedirect.com/science/article/pii/S0920410518302109

[6] S. Omar and D. Jiao, "A New Volume Integral Formulation for Broadband 3-D Circuit Extraction in Inhomogeneous Materials With and Without External Electromagnetic Fields," *IEEE Transactions on Microwave Theory and Techniques*, vol. 61, no. 12, pp. 4302–4312, Dec. 2013, conference Name: IEEE Transactions on Microwave Theory and Techniques.

[7] M. Bjelogrlic, M. Mattes, I. Koufogiannis, S. Capdevila, and J. R. Mosig, "Volume integral equation formulation for medical applications," in *9th European Conference on Antennas and Propagation (EuCAP)*, April 2015.

[8] P. De Tillieux and Y. Goussard, "Improving the Computational Cost of Image Reconstruction in Biomedical Magnetic Induction Tomography Using a Volume Integral Equation Approach," *IEEE Transactions on Antennas and Propagation*, pp. 1–1, 2020. [Online]. Available: https://ieeexplore.ieee.org/document/9142374/

[9] J. E. C. Serralles, R. Lattanzi, I. I. Giannakopoulos, B. Zhang, C. Ianniello, M. A. Cloos, A. G. Polimeridis, J. K. White, D. K. Sodickson, and L. Daniel, "Noninvasive Estimation of Electrical Properties From Magnetic Resonance Measurements via Global Maxwell Tomography and Match Regularization," *IEEE Transactions on Biomedical Engineering*, vol. 67, no. 1, pp. 3–15, Jan. 2020. [Online]. Available: https://ieeexplore.ieee.org/document/8673893/

[10] J. Lee, "Volume integral equation method for multiple isotropic inclusion problems in an infinite solid under tension or in-plane shear," *Journal of Mechanical Science and Technology*, vol. 24, no. 12, pp. 2529–2537, Dec. 2010. [Online]. Available: https://doi.org/10.1007/s12206-010-0917-z

[11] J. Lee and M. Han, "Three-Dimensional Volume Integral Equation Method for Solving Isotropic/Anisotropic Inhomogeneity Problems," *Mathematics*, vol. 8, no. 11, 2020. [Online]. Available: https://www.mdpi.com/2227-7390/8/11/1866

[12] S. Jarvenpaa, M. Taskinen, and P. Yla-Oijala, "Singularity extraction technique for integral equation methods with higher order basis functions on plane triangles and tetrahedra," *International Journal for Numerical Methods in Engineering*, vol. 58, no. 8, pp. 1149–1165, 2003.

[13] M. Khayat and D. Wilton, "Numerical evaluation of singular and near-singular potential Integrals," *IEEE Transactions on Antennas and Propagation*, vol. 53, no. 10, pp. 3180–3190, Oct. 2005. [Online]. Available: http://ieeexplore.ieee.org/document/1514571/

[14] R. R. Chang, K. Chen, J. Wei, and M. S. Tong, "Reducing Volume Integrals to Line Integrals for Some Functions Associated with Schaubert–Wilton–Glisson Basis Function," *IEEE Transactions on Antennas and Propagation*, vol. 69, no. 5, pp. 3033–3038, May 2021.

[15] L. Knockaert, "On the Analytic Calculation of Multiple Integrals in Electromagnetics," in *2011 International Conference on Electromagnetics in Advanced Applications*, Sep. 2011, pp. 595–598.

[16] E. H. Bleszynski, M. K. Bleszynski, and T. Jaroszewicz, "Reduction of Volume Integrals to Nonsingular Surface Integrals for Matrix Elements of Tensor and Vector Green Functions of Maxwell Equations," *IEEE Transactions on Antennas and Propagation*, vol. 61, no. 7, pp. 3642–3647, Jul. 2013.

[17] D. Schaubert, D. R. Wilton, and A. Glisson, "A tetrahedral modeling method for electromagnetic scattering by arbitrarily shaped inhomogeneous dielectric bodies," *IEEE Transactions on Antennas and Propagation*, vol. 32, no. 1, pp. 77–85, 1984.

[18] I. P. Georgakis and A. G. Polimeridis, "Reduction of volume-volume integrals arising in galerkin JM-VIE formulations to surface-surface integrals," in *11th European Conference on Antennas and Propagation (EuCAP)*, April 2017.

[19] M. T. Homer Reid, "Taylor–Duffy method for singular tetrahedron-product integrals: Efficient evaluation of galerkin integrals for VIE solvers," *IEEE Journal on Multiscale and Multiphysics Computational Techniques*, vol. 3, pp. 121–128, 2018.

[20] J. Rivero, F. Vipiana, D. R. Wilton, and W. A. Johnson, "Evaluation of 4-D Reaction Integrals Via Double Application of the Divergence Theorem," *IEEE Transactions on Antennas and Propagation*, vol. 67, no. 2, pp. 1131–1142, Feb. 2019.

[21] D. Wilton, F. Vipiana, and W. Johnson, "Evaluation of 4-D Reaction Integrals in the Method of Moments: Co-planar Element Case," *IEEE Transactions on Antennas and Propagation*, vol. 65, no. 5, pp. 2479–2493, May 2017.

[22] J. Rivero, F. Vipiana, D. R. Wilton, and W. A. Johnson, "Reducing the dimensionality of 6-D MoM integrals applying twice the divergence theorem," in *14th European Conference on Antennas and Propagation (EuCAP)*, March 2020.

[23] ——, "Acceleration of volume-volume 6-D integrals for numerical evaluation by double application of the divergence theorem," in *2019 International Applied Computational Electromagnetics Society Symposium (ACES)*, April 2019.

[24] ——, "6-D Integrals for Numerical Evaluation by Double Application of the Divergence Theorem," in *IEEE International Symposium on Antennas and Propagation*, July 2019.

[25] ——, "Fully numerical evaluation of galerkin interactions: Volumetric element case," in *IEEE International Symposium on Antennas and Propagation*, Fajardo, Puerto Rico, June 2016.

[26] A. G. Polimeridis, F. Vipiana, J. R. Mosig, and D. R. Wilton, "DIRECTFN: Fully Numerical Algorithms for High Precision Computation of Singular Integrals in Galerkin SIE Methods," *IEEE Transactions on Antennas and Propagation*, vol. 61, no. 6, pp. 3112–3122, Jun. 2013.

[27] Wolfram Research Inc., "Mathematica, Version 11.3," Champaign, IL, 2018. [Online]. Available: https://www.wolfram.com/mathematica

[28] D. Tihon and C. Craeye, "All-Analytical Evaluation of the Singular Integrals Involved in the Method of Moments," *IEEE Transactions on Antennas and Propagation*, vol. 66, no. 4, pp. 1925–1936, Apr. 2018.

[29] R. Graglia, "On the Numerical Integration of the Linear Shape Functions Times the 3-D Green's Function or its Gradient on a Plane Triangle," *IEEE Transactions on Antennas and Propagation*, vol. 41, no. 10, pp. 1448–1455, Oct. 1993.

[30] S. Tao and R. Chen, "A Higher-Order Solution of Volume Integral Equation for Electromagnetic Scattering From Inhomogeneous Objects," *IEEE Antennas and Wireless Propagation Letters*, vol. 13, pp. 627–630, 2014. [Online]. Available: http://ieeexplore.ieee.org/document/6775288/

[31] Q.-M. Cai, Y.-W. Zhao, Y.-T. Zheng, M.-M. Jia, Z. Zhao, and Z.-P. Nie, "Volume Integral Equation With Higher Order Hierarchical Basis Functions for Analysis of Dielectric Electromagnetic Scattering," *IEEE Transactions on Antennas and Propagation*, vol. 63, no. 11, pp. 4964–4975, Nov. 2015. [Online]. Available: http://ieeexplore.ieee.org/document/7275147/